ACS APPLIED ENERGY MATERIALS

Article

On the Growth of Ordered Iron Oxide Nanowires for Photoelectrochemical Water Oxidation

Julian Moreno, Mohd Adnan Khan, Yurii P. Ivanov, Sergei Lopatin, Jorge A. Holguin-Lerma, Giovanni Marinaro, Boon S. Ooi, Hicham Idriss, and Jürgen Kosel

ACS Appl. Energy Mater., **Just Accepted Manuscript** • DOI: 10.1021/acsaem.9b01343 • Publication Date (Web): 10 Oct 2019

On the Growth of Ordered Iron Oxide Nanowires for Photoelectrochemical Water Oxidation

Julián A. Moreno †, M.A. Khan[*] [‖], Yurii P. Ivanov ‡ [♯], Sergei Lopatin [⊥], Jorge A. Holguín-Lerma ‡, Giovanni Marinaro ‡ [ξ] [Δ], Boon S. Ooi ‡, Hicham Idriss [‖], and Jürgen Kosel*[*] *‡.*

† King Abdullah University of Science and Technology (KAUST), Physical Science and Engineering Division (PSE), Thuwal 23955-6900, Saudi Arabia

‖ SABIC Corporate Research and Development Center, Saudi Arabia

‡ King Abdullah University of Science and Technology (KAUST), Computer, Electrical and Mathematical Science and Engineering Division (CEMSE), Thuwal 23955-6900, Saudi Arabia

♯ Department of Materials Science & Metallurgy, University of Cambridge, Cambridge CB3 0FS, UK

⊥ King Abdullah University of Science and Technology (KAUST), Core Labs, Thuwal, 23955-6900, Saudi Arabia

KEYWORDS: STEM; EELS; nanowires; photoelectrochemical; water oxidation

ABSTRACT

This work reports the synthesis of ordered and vertically aligned iron oxide nanowires for photoelectrochemical (PEC) water oxidation. The nanowires exhibited promising PEC activity for water oxidation with saturated photocurrents of ~0.8 mA cm^{-2} at 1.23 V vs RHE. Various factors inevitably affect their photochemical activity such as crystallinity, morphology, compositional gradient, and surface states. They were studied with HRTEM, EELS and Raman shift techniques. The nanowires had complex compositional and morphological structures at the nano and atomic scales. The nanowires annealed at 350 ^{0}C had an outer shell dominated by Fe^{3+} cations, while the core had mixed oxidation

states of iron cations (+2 and +3). In contrast, nanowires annealed at 450 ^{0}C are fully oxidized with Fe^{3+} cations only and were found to be more active. At the same time, we observed anisotropic compositional gradients of nickel cations inside of the iron oxide, originating from the nickel support film. Our work shows that the methodology used can affect the composition of the surface and near surface of the grown nanowires. It therefore points out the importance of a detailed analysis, in order to obtain a realistic structure-activity relationship in photo-electro-catalysis.

INTRODUCTION

Hematite (α-Fe_2O_3) has long been considered a promising material for photocatalytic water oxidation. An appropriate band gap (~2.0 – 2.2 eV) and valence band edge (~ 2.6 V vs normal hydrogen electrode (NHE) @ pH = 0) makes it an ideal candidate for this reaction. Yet, its poor charge transport primarily due to a small diffusion length hinders its activity. Ultra-fast dynamics of charges in the excited states in hematite thin films and single crystals have shown that their lifetime is in the order of a few picoseconds. [1,2] This

short lifetime and small diffusion length of < 20 nm [3,4] have spurred the exploration of nanostructure effects for improving the photocatalytic activity of hematite.

Colloidal α-Fe_2O_3 nanoparticles (~ 60 nm) have been shown to have much better photocatalytic performance than single crystals or sintered powder. [5–8] However, colloidal particles/nanopowders cannot split water, as α-Fe_2O_3 needs a small bias voltage for overall water splitting, because its conduction band edge is below the hydrogen reduction potential. A more practical approach to water splitting is to use a photo-electro-chemical (PEC) cell with α-Fe_2O_3 as the photoanode, so the needed bias can be applied for overall water splitting. In that respect, thin films of α-Fe_2O_3 (< 20 nm thick) have been studied [6] and found to be impractical, due to their poor absorptivity. Thicker but porous films were also prepared and tested, showing low activity with an Incident Photon to Current Efficiency (IPCE) around 1%. [7] The higher quantum efficiency of similar particles, when dispersed in an electrolyte, indicated that boundaries between the particles had a negative effect on charge carrier recombination rates, and thus resulted in poor activity. [8] A promising solution avoiding the problem of grain boundaries in α-Fe_2O_3 films is the use of nanowires.

Various techniques have been used to synthesize crystalline α-Fe_2O_3 nanowires (to circumvent some of the above shortfalls) for photocatalytic applications such as hydrothermal synthesis, [5] heating iron foils [9] and spray pyrolysis. [10] However, these techniques do not have a good control over size or density of the nanowire array. Among the various methods for fabrication of nanowires, the anodized aluminum oxide (AAO) template-assisted electrodeposition technique has been widely used in the preparation of a wide range of metallic, semiconductor, and polymeric nanowires. [11] Using this method, it is easier to control the size, shape, and structural properties of nanowires through the modification of templates and electrodeposition conditions, making it an attractive option for many applications. [12–15] Moreover, the high density and the ordered structure of nanowires, when using the AAO method, has several other advantages, including light trapping by photonic crystals, for example. [16,17] Nevertheless, there have been limited studies on the synthesis of iron oxide nanowires using AAO templates for photocatalytic applications. [18–20] The best reported iron oxide (without doping) nanowires activity made using AAO templates had a saturation photocurrent of ~ 1.0-1.5 mA cm^{-2} @ 1.23 V vs reversible hydrogen electrode (RHE). [18,19,21] In this work, we have grown iron oxide

nanowires using AAO templates, tested their PEC activity and studied the various factors poised to affect their photochemical activity including morphology, compositional gradient, and surface states using scanning electron microscopy (SEM), Raman spectroscopy, scanning transmission electron microscopy (STEM) and Electron Energy Loss Spectroscopy (EELS).

METHODS

Porous alumina templates were fabricated by mild anodization of aluminum in an aqueous oxalic acid electrolyte, [22,23] as seen in **Figure 1**a. On one side of the template, a 100 nm layer of gold was sputtered (**Figure 1**b) to act as electrode for the subsequent electrodeposition, which was carried out galvanostatically with a (60 g L^{-1}) iron sulfate ($FeSO_4 \cdot 7\ H_2O$), (10 g L^{-1}) boric acid (H_3BO_3) and (10 g L^{-1}) ascorbic acid ($C_6H_8O_6$) aqueous electrolyte (**Figure 1**c). This resulted in the formation of cylindrical iron (Fe) nanowires inside of the template. After this, a layer of nickel (Ni) was electroplated on the back side of the template, i.e. on top of the sputtered gold (**Figure 1**d), using a Watts solution [24] containing (300 g L^{-1}) nickel sulfate ($NiSO_4 \cdot 6H_2O$), (45 g L^{-1}) nickel chloride

($NiCl_2 \cdot 6H_2O$) and (40 g L^{-1}) boric acid (H_3BO_3). This Ni layer, with a linear temperature expansion coefficient of ~ 13.0 x 10^{-6} m (m K) $^{-1}$, matches closely the one of gold ~ 14.0 x 10^{-6} m (m K) $^{-1}$ and iron ~ 13.0 x 10^{-6} m (m K) $^{-1}$, [25] working as mechanical support.

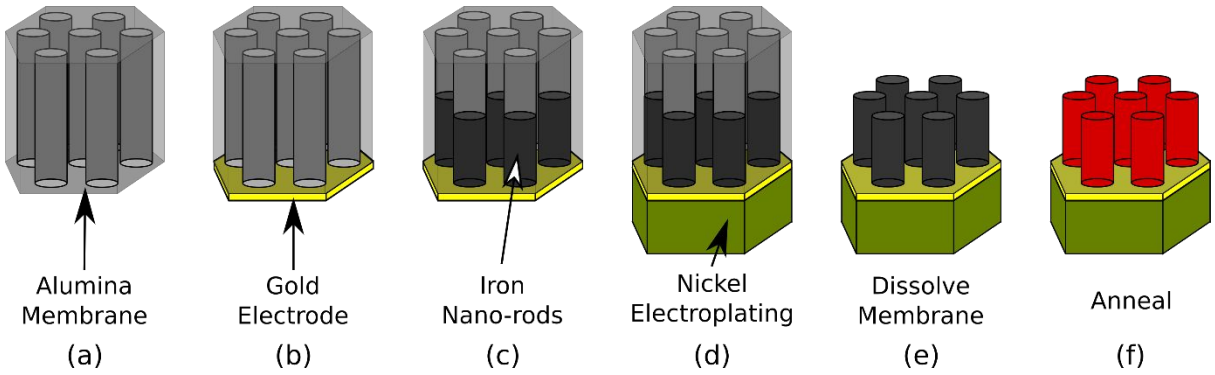

Figure 1. A schematic description of the synthesis process of iron oxide nanowires. Starting from an alumina template (a), a thin gold layer was sputtered to serve as electrode (b) for a subsequent iron electroplating (c). Nickel was electroplated over the gold electrode (d) as mechanical support for the nanowires. After dissolution of the template, free-standing nanowires were obtained (e) and annealed (f) to get iron oxide nanowires.

After that, the template was etched in an aqueous solution of (18 g L^{-1}) chromium trioxide (CrO_3) and (57.6 g L^{-1}) phosphoric acid (H_3PO_4), leaving the bare wires standing

perpendicular to the surface (**Figure 1**e). Finally, the bare Fe nanowires were annealed at different temperatures of 250, 350, 450 and 550°C in air (for 2 hours) for which a heat ramp of 2°C min^{-1} was used (**Figure 1**f). The samples were left to cool down inside the closed oven, until the temperature was below 40°C.

For morphological characterization (diameter, height, etc.), SEM images with similar magnification were obtained in a FEI Nova Nano SEM with a 5 kV acceleration voltage and 2.5 spot size. All samples were imaged from the top and at a 30° tilt angle.

Elemental analysis of isolated nanowires was performed with a dedicated scanning transmission electron microscope (STEM) at an energy of 300 kV, equipped with a post-column high-resolution Gatan energy loss spectrometer. The single spectra of Fe L and O K edges were also acquired with an energy resolution of 0.18 eV, from 400 to 900 eV. The EELS images were recorded with a 1.5 nm scan step and a 1 s exposure time. For the cross-section preparation of the nanowires, a focused ion beam “lift-out” protocol was used. [26]

Raman analysis of the samples was performed using a Thermo Scientific™ DXR™ Raman spectrometer with a 532 nm wavelength, 3 mW power, 0.7 mm spot size laser,

an aperture opening of 50 mm and a grating of 900 lines per mm. The samples were analyzed from 100 to 2000 cm^{-1} and averaged over 16 scans from different points in the sample.

The PEC testing of iron oxide nanowires was carried out using a multi-channel Bio-Logic VSP-300 potentiostat in a three-electrode setup. The iron oxide nanowires were used as the working electrode, a platinum (Pt) mesh as a counter electrode and silver/silver chloride (Ag/AgCl) as a reference electrode. The cyclic voltammetry (CV) was performed with a sweeping voltage @ 20 mV s^{-1}. The iron oxide photoanodes were prepared by connecting a copper foil to the Au film below the nanowires. Since the alumina templates are grown with non-anodized aluminum as a frame, the sample was covered and sealed in epoxy so that only the iron oxide nanowires were exposed to the electrolyte. The potential of the working electrode (iron oxide nanowires) is reported against the RHE by the Nernstian equation: $V_{RHE} = V_{AgCl} + 0.059\, pH + V^{o}_{AgCl}$, with $V^{o}_{AgCl} = 0.197\, V$ at room temperature.[27]

RESULTS AND DISCUSSION

Figure 2(a-d) shows the top view SEM images of the as-prepared bare Fe nanowires with

comparable magnification. An average diameter of ~60 nm and density of 10^{10} nanowires per

cm^2 was measured using imageJ software. [28] After annealing in air at 250°C, 350°C, 450°C or

550°C for two hours (**Figure 2**(e-h), respectively), the diameter increased while the height decreased logarithmically as seen in **Figure 2**(m) and (n). By estimating, the volumes of representative wires as cylinders from each sample, a nearly two-fold volume expansion was found

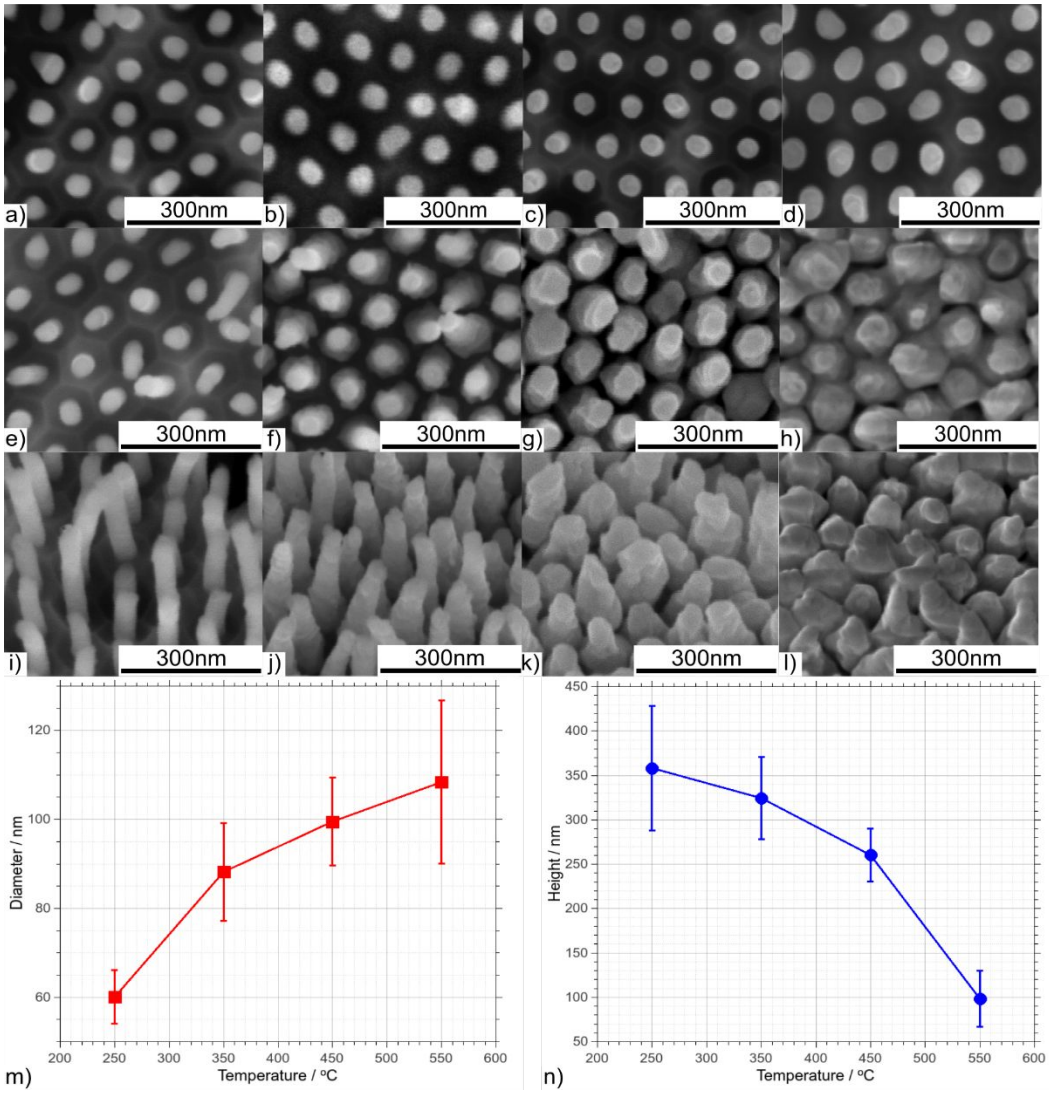

Figure 2. SEM images of iron oxide nanowire arrays. Top view of as-prepared bare nanowires (a-d) and bare nanowires annealed in air at 250°C (e), 350°C (f), 450°C (g), and 550°C (h) for two hours. Tilted view of annealed bare nanowires (i-l). Diameter (m) and height (n) evolution for samples annealed at different temperatures.

for the samples annealed at 350°C and 450°C. This effective doubling of the volume is consistent with the calculated Pilling–Bedworth ratio (P–B ratio) which is ~ 2.1 for magnetite and 2.14 for hematite. [29] It is important to note that, as will be seen below, this volume expansion could be misleading in assigning the iron oxide phase and that the diameter of the iron oxide nanowires annealed at 350°C and 450°C is much higher than the diffusion length of α-Fe_2O_3 (~ 20 nm).[3,4] The sample annealed at 550°C (**Figure 2**(h, l)) is sintered, i.e., the nanowires have lost most of their cylindrical shape and are in contact with their neighbors.

The PEC activity of the iron oxide nanowires was evaluated using linear sweep voltammetry (LSV) in a three-electrode setup without uncompensated resistance correction. The three-electrode setup consists of a Pt counter electrode and a standard Ag/AgCl reference electrode in 1.0 M KOH (pH ~ 14) electrolyte. The sample annealed at 250°C did not show any photo response, while the sample annealed at 550°C was not considered for testing, due to sintering, as seen in **Figure 2**. The LSV curves shown in **Figure 3** reveal an onset potential around 1.0 V and 0.8 V vs RHE for samples annealed

at 350 °C and 450 °C, respectively. This is higher than the flat band potential of α-Fe_2O_3, which is around 0.4-0.6 V vs RHE. [30,31] This higher onset potential needed for α-Fe_2O_3 is attributed to the recombination of bulk hematite electrons with holes at the semiconductor/electrolyte interface. [30] At low anodic bias, the energetic barrier generated by the space charge layer is not strong enough to prevent this recombination and a stronger anodic bias (~ 500 mV anodic of flat band) is needed. Because of this, water oxidation primarily happens at higher potentials (around 0.8 – 1.0 V vs RHE) than hematite's flatband potential, even for the single crystal electrodes. [32] The samples annealed at 350 °C have a lower activity (around 40% less at 1.23 V vs RHE) than the samples annealed at 450 °C. A saturated photocurrent of about 0.8 mA cm^{-2} at 1.23 V vs RHE for the 450 °C sample is found, which is similar to the activity reported for iron oxide single crystals and powders. [7,9,10,32] Nonetheless, it is lower than some other forms of nanostructured iron oxide made using CVD. [27] Although it is difficult to compare PEC activity as it depends on many factors (e.g. crystallinity, morphology, doping, light flux, co-catalyst and electrolyte pH), the reader may find a short summary of reported

photocurrent values at 1.23 V vs RHE of undoped iron oxide nanostructures without any co-catalysts in supplementary **Table S1.**

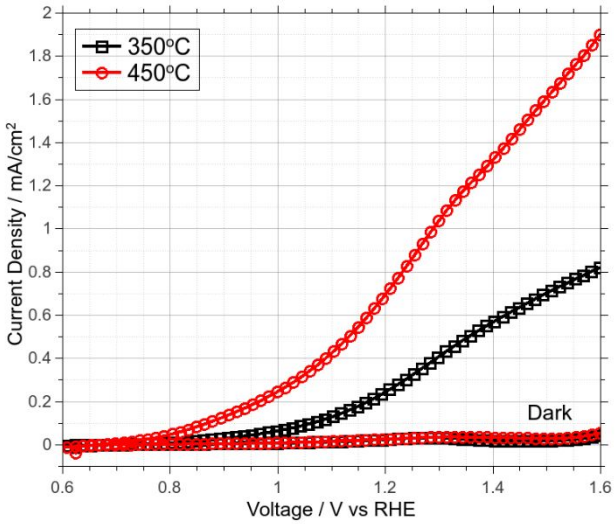

Figure 3. Linear sweep voltammetry of iron oxide nanowires annealed in air at 350°C and 450°C for 2 hours. Experimental conditions: Three-electrode system in 1M KOH (pH 14) under 1.5 suns illumination and a Pt counter electrode for hydrogen evolution reaction.

To elucidate the crystalline phase obtained after the annealing process, Raman spectroscopy was conducted, as shown in **Figure 4**. **Table 1** lists the reported Raman vibrational modes expected from iron oxides. The spectra for samples annealed at 350, 450 and 550°C have peaks at 224, 244, 292, 410, 497, 611 and 1318 cm^{-1}, which can

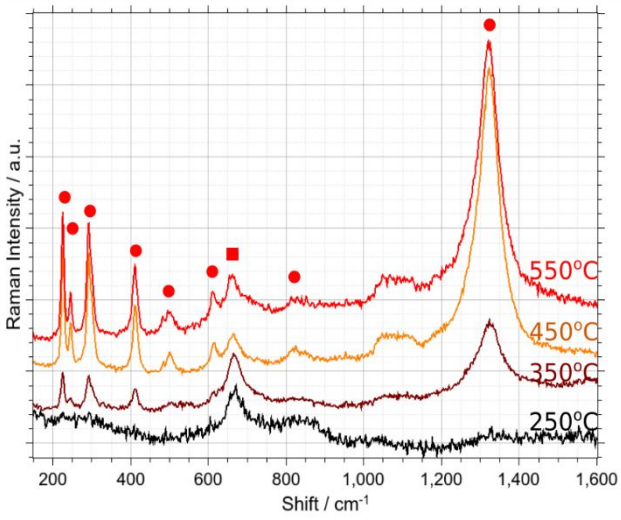

Figure 4. Raman spectra of annealed iron nanowires at temperatures of 250˚C, 350˚C, 450˚C and 550˚C for 2 hours. Solid circles correspond to hematite peaks; the solid square corresponds to a magnetite peak.

be assigned to the α-Fe_2O_3 crystallographic phase. [10] These peaks have been marked with solid circles in **Figure 4**. The peaks at 224 and 497 cm^{-1} are assigned to the A_{1g} mode, while all other peaks at 244, 292, 410 and 611 cm^{-1} can be assigned to the E_g mode. The peak at 656 cm^{-1} corresponds to a secondary phase; it may be Fe_3O_4, FeO, or γ-Fe_2O_3, since all three compounds exhibit a peak around 658 cm^{-1}. [33,34] However, γ-Fe_2O_3 has a doublet at 667 and 718 cm^{-1}. Moreover, as FeO and γ-Fe_2O_3 are not stable at room temperature; [34] they are unlikely to be present in the samples. Hence, the peak

at 656 cm^{-1} is probably due to Fe_3O_4. At 250 °C annealing temperature, only the Fe_3O_4 phase is detected. The peak at 1320 cm^{-1} is assigned to the $2E_u$ (LO) mode and originates from a two-phonon scattering that is known to be resonantly enhanced. [35,36] With increasing temperatures, a decrease in the Fe_3O_4 peak and the appearance followed by increase in intensities of α-Fe_2O_3 vibrational modes is observed.

Table 1. Identification of Raman peaks in iron oxide

Peaks [cm^{-1}]	Crystallographic phase	Raman active phonon mode [35–37]
224	α-Fe_2O_3	A_{1g}
244	α-Fe_2O_3	E_g
292	α-Fe_2O_3	E_g
409	α-Fe_2O_3	E_g
497	α-Fe_2O_3	A_{1g}
611	α-Fe_2O_3	E_g

656	Fe_3O_4	A_{1g}
1318	α-Fe_2O_3	2nd order scattering peak

To understand the oxidation process, a single nanowire annealed at 350°C was studied with a combination of STEM and EELS. High-resolution electron-energy loss near-edge fine structure is known to provide information on the local structure and bonding. **Figure 5**a shows a High Angle Annular Dark Field (HAADF) cross-sectional STEM image of oxidized Fe nanowires, prepared by a focused ion beam process in which the nanowire section is shown in dark gray encircled with the dashed dark blue line. Platinum can be

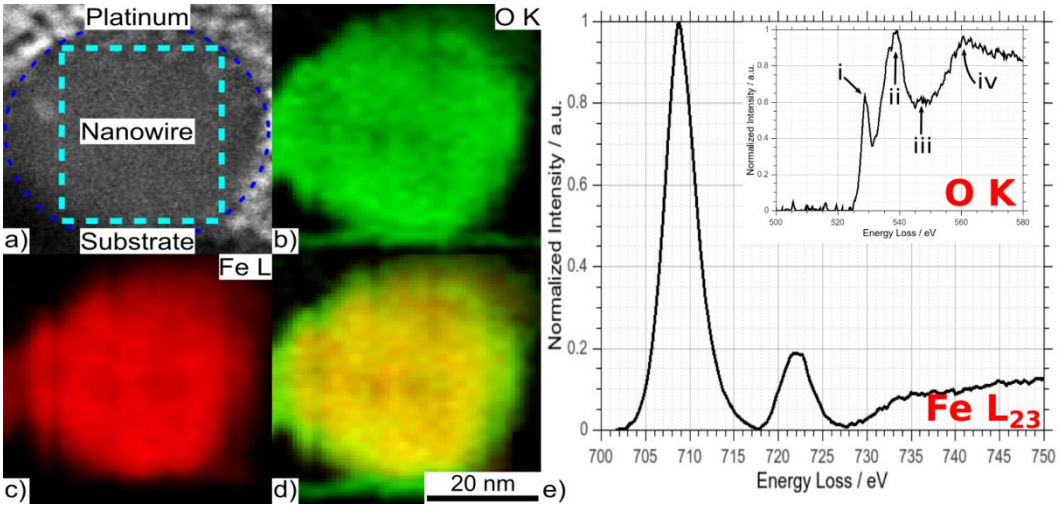

Figure 5. Cross section of a nanowire: (a) High angle annular dark field STEM image and compositional mappings of oxygen (b), iron (c) and their superposition (d) obtained with monochromatic electron energy loss spectroscopy of the cross section of a nanowire annealed at 350°C (e) Electron Energy Loss Spectra at the oxygen K-edge (inset) and the

seen in light gray on the upper part of the subfigure (covering the nanowire) and the silicon oxide substrate is shown at the bottom. The atomic composition in the sample is studied by filtering electrons with a specific energy loss. In **Figure 5**b, from the oxygen (O) K-edge compositional mapping, it is clear that oxygen is present throughout the cross-section indicating complete oxidation of the nanowire core. **Figure 5**c shows the Fe L-edge compositional mapping and **Figure 5**d the superposition of **Figure 5**b and c, revealing a fully oxidized nanowire in iron oxide state. The green circle around the nanowires in **Figure 5**d shows that the surface of the wire is oxygen-dominated as it appears also from the silicon oxide substrate in **Figure 5**b.

Figure 5e shows the Fe $L_{2,3}$ edge spectra and O K-edge spectra (inset) taken from the dashed square in **Figure 5**a. The EELS fine structure of the O K (~ 530 eV) and the Fe $L_{2,3}$ (~710 eV) energy edges can be used to identify a specific iron oxide phase. The O K spectrum has features labeled as (i), (ii), (iii) and (iv) in the inset of **Figure 5**e. The pre-peak (i), located around 530 eV can be interpreted as electronic transitions from the O 1s core state to the unoccupied states of O 2p hybridized with the Fe 3d states. [38,39] The (ii), (iii) and (iv) peaks are due to the transition of the O 1s electrons to O 2p unoccupied

states hybridized with Fe unoccupied 4s and 4p states. [39] Peak (ii) is the dominant peak around 540 eV which remains rather similar for FeO, Fe_3O_4, γ-Fe_2O_3, and α-Fe_2O_3. Peak (iii) is very weak and peak (iv) is a rather broad peak and without any characteristic profile. [38,39] The relative peak position and intensity ratio of pre-peak (i) to peak (ii) can be used to identify the oxide phase. From the inset of **Figure 5**e, the relative position of peak (i), relative to (ii) is 10.04 eV, which would classify the phase as Fe_3O_4 (magnetite), according to Colliex et. al. [38] The intensity ratio of peak (i) with respect to (ii) was found to be ~0.66 which is similar to what was reported by Wang et. al. for pure Fe_3O_4 nanocrystals.[39]

The Fe $L_{2,3}$ edges can be used to identify the specific iron oxide phase. The intense peaks (white lines) on the Fe $L_{2,3}$ edges are due to strong $2p^63d^n \rightarrow 2p^53d^{n+1}$ excitations (n=5 for Fe^{3+} and n=6 for Fe^{2+}) and are labeled as L_3 (~ 709 eV) and L_2 (~ 722 eV).[38–40] The valence state of Fe can be determined from the following three aspects of the Fe $L_{2,3}$ EELS fine structure: chemical shift (the energy edge position), fine structural features (splitting of the peaks), and the white-line ratios of the Fe L_2 and Fe L_3 spectra. The separation of the L_3 and the L_2 maxima due to the spin-orbit splitting was reported as 13 ± 0.3 eV in all iron oxides [38–42] therefore, this separation can be used for calibration

purposes only. However, the white-line intensity ratio $I(L_3)/I(L_2)$ in the 3d Fe is valence dependent; therefore, this ratio can be used to distinguish between different iron oxide phases. The reported L_3/L_2 ratios have a dependence on the origin of the samples and data analysis method, and vary slightly in different studies. For example, Colliex et. al. [38] reported that these ratios range from 3.9 to 4.6 for FeO, 4.2 to 5.3 for Fe_3O_4 and from 4.8 to 6.5 for α-Fe_2O_3, depending on the intensity analysis method. Cavé et. al. [41] reported L_3/L_2 ratios to be ~ 5.0 for Fe_3O_4 and 5.7 for α-Fe_2O_3. Gunay et. al. [42] also observed L_3/L_2 ratios of ~ 4.2 for FeO, 4.5-5.3 for Fe_3O_4 and 5.5-6.9 for α-Fe_2O_3. Regardless of the analysis method, their ratio increases with increasing Fe valence state. [42] The Fe L_2 and L_3 peak maxima from the core of the nanowire are at 722 eV and 709 eV, respectively, as shown in **Figure 5**e. This energy difference of ~ 13.0 eV is identical to reported values for various iron oxide phases. [38–42] The calculated white-line ratio of the Fe L_2 and Fe L_3 edge was ~ 5.0, indicating the core of the nanowires annealed at 350^0C has Fe in mixed oxidation state (+2 and +3) or in other words iron oxide is probably in the Fe_3O_4 phase.[43]

To further analyze the oxidation process, we performed side view EELS of the nanowires annealed at 350^{0}C and 450^{0}C. The EELS spectra were analyzed in regions ranging from their edge (boxes 1 and 4) to their center, (boxes 3 and 6), as shown in **Figure 6**a and b. The Fe L-edge spectra can be found in supporting **Figure S1** for all boxes. The Fe L-edge white line ratios were calculated and their results are plotted in **Figure 6**c. Based on changes in the Fe L-edge ratios it appears that the edge of both nanowires annealed at 350^{0}C and 450^{0}C is dominated by Fe^{3+} cations i.e. the outer shell is completely oxidized as indicated by L_3/L_2 ratio of ~ 5.3 and 5.2, respectively. In case of

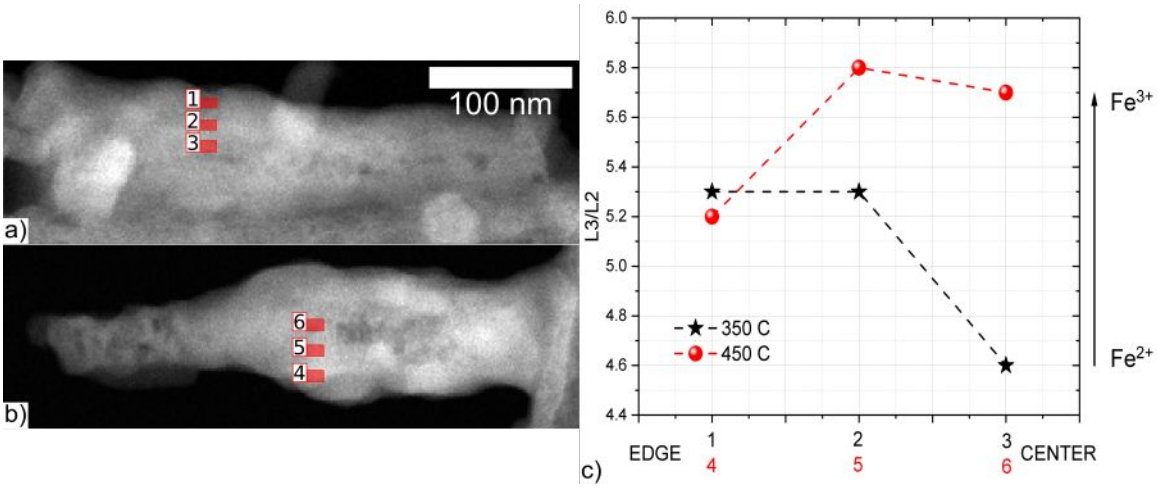

Figure 6. HAADF STEM images of released nanowires annealed at 350 oC (a) and 450 oC (b). The inset boxes represent areas, where EELS spectra were taken from. (c) White line ratios of the iron L-edge calculated from the spectra extracted from the inset boxes (x-axis). Raw data can be found in supplementary **Figure S1**.

the sample annealed at 350^0C, when moving towards the center the L_3/L_2 ratio decreases suggesting decrease in the overall Fe valence state from +3 to +2; in line with the interpretation of data reported in **Figure 5**. In contrast, the nanowire annealed at 450^0C is fully oxidized with an overall L_3/L_2 ratio of ~5.7 in the center. The difference in Fe valence state in boxes 3 and 6 shows the different rates at which oxygen diffuses inwards with different annealing temperatures. At annealing temperatures of 450^0C fully oxidized nanowires are obtained in α-Fe_2O_3 phase (Fe:+3 oxidation state), while at 350^0C the shell is composed of an α-Fe_2O_3 phase (Fe:+3) and the core is of Fe_3O_4 phase (two Fe in +3 and one Fe in +2 oxidation sates). This could explain the lower PEC activity of the nanowires annealed at 350^0C compared to those annealed at 450^oC [31,44–46] , and the increased diffuse reflectance of a more oxidized structure as it approaches transparency at wavelength energies below the α-Fe_2O_3 bandgap (~2.2 eV, ~560 nm). [47] (see supplementary **Figure S3**).

Figure 7 presents side views of compositional energy-filtered mappings obtained by EELS from nanowires annealed at 350°C (7a) and 450°C (7b) with the bottom end of the nanowire at the left side of each inset. The top left is a high angle annular dark field image with the energy filtered mappings of oxygen, iron, nickel and chromium below, and the

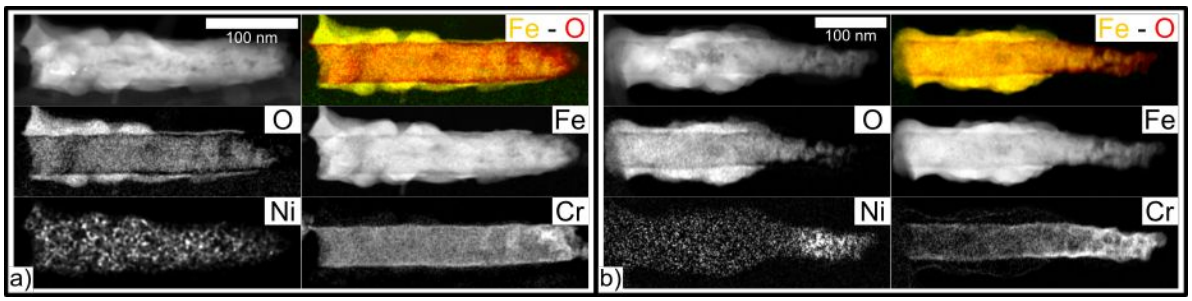

Figure 7. Compositional maps of nanowires annealed at 350 oC (a) and 450 oC (b) with their bottom end at the left-hand side (growing direction from left to right side). The top left corresponds to the HAADF STEM image. Below, the gray-scale energy filtered mappings of oxygen, iron, nickel and chromium are shown. The top right image is a colored superposition of iron and oxygen mappings only.

top right is a colored superposition of iron and oxygen only. As mentioned in the methods section, a Ni film is used as a mechanical support for the vertically standing nanowires and a solution of chromium trioxide (CrO_3) in phosphoric acid (H_3PO_4), was used to etch

the alumina template. The bright grey spots on each image represent the respective elements. From **Figure 7**, we can make several observations. Firstly, the oxygen mapping image indicates that the oxygen concentration at the core of the nanowire annealed at 450°C is higher than the one annealed at 350°C. This is in line with the discussion of **Figure 5** and **Figure 6**. Secondly, the Fe mapping image suggests that upon annealing, Fe at the bottom of the nanowire expands to the sides. This could be explained by the outward diffusion of Fe ions, since the growth of the oxide layer on Fe happens at the oxide-gas interface following the Caberra-Mott theory [48,49] and the inwards diffusion of Ni.

During the oxidation of iron, the Fe outward diffusion is the dominant mass transport process. [49] In Fe nanostructures, this leads to formation of voids at the metal/metal oxide interface, even at room temperature [49,50] allowing the formation of hollow structures. This is associated with the Kirkendall effect [51,52] by which the outward diffusion rate of Fe is much larger than the inward diffusion rate of oxygen. This has been observed for both Fe nanoparticles and nanowires. [49–51] At the same time high temperature (>700 K) oxidation leads to shrinkage and collapse of the nanostructures due to growth and increase of voids

[49,51] which could explain the shrinkage and collapse of the Fe nanowires annealed at 550^0C as observed in **Figure 2** h & l.

Figure 7 also shows the diffusion on nickel into the nanowires from the bottom, through the porous gold layer (see supplementary **Figure S2**). The diffusion coefficient (D) in solids at different temperatures is generally well predicted by the Arrhenius equation. If we consider that Ni ions are diffusing in three dimensions, then using Einstein's approximation we can approximate the time it takes to diffuse an average distance in one dimension using:

$$t = \frac{x^2}{2D} \quad (1)$$

where x is the mean distance traveled by the diffusing ion along one axis after an elapsed time t. Using an annealing time of 2 hours (7200 s) we calculated the diffusion coefficient of Ni along the length of the nanowires (x ~ 260 nm) using equation (2) as 4.69 $nm^2\ s^{-1}$ or 4.69 x $10^{-18}\ m^2\ s^{-1}$. Comparable values can be found for the diffusion of Ni in other iron oxides and pure iron phases. [53] Nickel cation diffusion in bulk magnetite has been reported by Eveno et. al. [54] as:

$$D = 4.32 \text{ x } 10^{-6} \exp\left(-\frac{196000}{RT}\right) \quad (2)$$

At annealing temperatures of 450^0C (723 K), equation (2) gives D = 3 x 10^{-20} m^2 s^{-1}. Hirano et. al. [55] measured nickel diffusion into ferromagnetic alpha-iron as:

$$D = 1.4\text{x } 10^{-4} \exp\left(-\frac{245600}{RT}\right) \quad (3)$$

At annealing temperatures of 450^0C (723 K), equation (3) gives D = 2.54 x 10^{-22} m^2 s^{-1}.

Thus, it is clear that Ni diffusion into the iron oxide nanowires is faster than in bulk systems. This is probably due to the formation of voids and the porous nature of the iron oxide nanowires during annealing as discussed above. Lastly, we also see the presence of chromium on the surface of the nanowires coming from the etching solution.

CONCLUSIONS

We have synthesized ordered iron oxide nanowires suitable for photoelectrochemical (PEC) water oxidation. Iron nanowires were synthesized using electrodeposition of iron cations in AAO templates, using a Au film as electrode on the bottom side and a Ni film for mechanical support. After removing the alumina template, an ordered array of free-standing iron nanowires was obtained on top of the Au/Ni substrate, a structure that may

serve different applications. Then, the nanowires were converted to iron oxide by annealing at temperatures above 350ºC in air. This caused doubling of the volume, in line with the expected Pilling–Bedworth ratio for Fe_3O_4 and α-Fe_2O_3. Raman spectroscopy also indicated that increasing the annealing temperature led to an increase of the α-Fe_2O_3 signal and a decrease of the Fe_3O_4 signal. STEM combined with EELS further elucidated the oxidation process. At annealing temperatures of 450ºC, the nanowires were completely oxidized in α-Fe_2O_3 phase, while at 350ºC it displayed a core-shell structure with a shell made of α-Fe_2O_3 and a core composed predominantly of Fe_3O_4. The samples annealed at 350ºC have a lower PEC activity (~ 40% less) than the samples annealed at 450ºC. The PEC activity (0.8 mA cm^{-2} at 1.23 V vs RHE) for the 450 ºC sample is similar to the activity reported for iron oxide single crystals and powders even though, upon annealing, nickel from the mechanical support film diffuses into the iron oxide nanowires. This takes place much faster compared to bulk systems and can be explained because of the formation of voids in iron nanostructures during annealing. This also contributes towards the doubling in volume mentioned before and should be taken into account when evaluating the morphology of metal oxide electrodes, regardless of the nickel diffusion.

This nickel diffusion into the voids of iron oxide nanostructures during annealing could be used as nanostructure alloying for different applications which, we have shown, differs from bulk. Lastly, we also see the presence of chromium on the surface of the nanowires coming from the etching solution. Whether the nickel and chromium affect the PEC activity positively or negatively, is yet to be understood.

ASSOCIATED CONTENT

The following files are available free of charge:

Selected iron L-edges spectra; sputtered gold on alumina template SEM image; diffuse reflectance measurements (docx)

AUTHOR INFORMATION

Corresponding Author

*khanmda@sabic.com, * jurgen.kosel@kaust.edu.sa.

Present Addresses

ξ Institute of Process Engineering and Environmental Technology, Technical University Dresden, 01062, Germany

Δ Institute of Fluid Dynamics, Helmholtz-Zentrum Dresden-Rossendorf, 01314, Germany

Author Contributions

The manuscript was written through contributions of all authors. All authors have given approval to the final version of the manuscript.

Notes

The authors declare no competing financial interest

ACKNOWLEDGMENTS

This publication is based upon work supported by the King Abdullah University of Science and Technology (KAUST) Office of Sponsored Research (OSR) under award No. OSR-2016-CRG5-2956.

REFERENCES

(1) Cherepy, N. J.; Liston, D. B.; Lovejoy, J. A.; Deng, H.; Zhang, J. Z. Ultrafast Studies of Photoexcited Electron Dynamics in γ- and α-Fe $_2$ O $_3$ Semiconductor Nanoparticles. *J. Phys. Chem. B* **1998**, *102* (5), 770–776. https://doi.org/10.1021/jp973149e.

(2) Joly, A. G.; Williams, J. R.; Chambers, S. A.; Xiong, G.; Hess, W. P.; Laman, D. M. Carrier Dynamics in α-Fe 2O 3 (0001) Thin Films and Single Crystals Probed by Femtosecond Transient Absorption and Reflectivity. *J. Appl. Phys.* **2006**, *99* (5). https://doi.org/10.1063/1.2177426.

(3) Sastri, M. V. C.; Nagasubramanian, G. Studies on Ferric Oxide Electrodes for the Photo-Assisted Electrolysis of Water. *Int. J. Hydrogen Energy* **1982**, *7* (11), 873–

876. https://doi.org/10.1016/0360-3199(82)90005-2.

(4) Kennedy, J. H.; Frese, K. W. Photooxidation of Water at α-Fe2O3 Electrodes. *J. Electrochem. Soc.* **1978**, *125* (5), 709–714. https://doi.org/10.1149/1.2131532.

(5) Yichuan Ling, Gongming Wang, Damon A. Wheeler, Jin Z. Zhang, and Y. L. Sn-Doped Hematite Nanostructures for Photoelectrochemical Water Splitting. *Nano Lett.* **2011**, 2119–2125. https://doi.org/10.1021/nl200708y.

(6) Itoh, K.; Bockris, J. O. M. Stacked Thin-Film Photoelectrode Using Iron Oxide. *J. Appl. Phys.* **1984**, *56* (3), 874–876. https://doi.org/10.1063/1.334028.

(7) Björkstén, U.; Moser, J.; Grätzel, M. Photoelectrochemical Studies on Nanocrystalline Hematite Films. *Chem. Mater.* **1994**, *6* (6), 858–863. https://doi.org/10.1021/cm00042a026.

(8) Moser, J.; Grätzel, M. Photoelectrochemistry with Colloidal Semiconductors; Laser Studies of Halide Oxidation in Colloidal Dispersions of TiO2 and A-Fe2O3. *Helv. Chim. Acta* **1982**, *65* (5), 1436–1444. https://doi.org/10.1002/hlca.19820650517.

(9) Wen, X.; Wang, S.; Ding, Y.; Lin Wang, Z.; Yang, S. Controlled Growth of Large-Area, Uniform, Vertically Aligned Arrays of ??-Fe 2O 3 Nanobelts and Nanowires. *J. Phys. Chem. B* **2005**, *109* (1), 215–220. https://doi.org/10.1021/jp0461448.

(10) Duret, A.; Grätzel, M. Visible Light-Induced Water Oxidation on Mesoscopic α-Fe 2O3 Films Made by Ultrasonic Spray Pyrolysis. *J. Phys. Chem. B* **2005**, *109* (36), 17184–17191. https://doi.org/10.1021/jp044127c.

(11) Lee, W.; Park, S.-J. Porous Anodic Aluminum Oxide: Anodization and Templated Synthesis of Functional Nanostructures. *Chem. Rev.* **2014**, *114* (15), 7487–7556. https://doi.org/10.1021/cr500002z.

(12) Yassine, O.; Zaher, A.; Li, E. Q.; Alfadhel, A.; Perez, J. E.; Kavaldzhiev, M.; Contreras, M. F.; Thoroddsen, S. T.; Khashab, N. M.; Kosel, J. Highly Efficient Thermoresponsive Nanocomposite for Controlled Release Applications. *Sci. Rep.* **2016**, *6*, 1–7. https://doi.org/10.1038/srep28539.

(13) Alfadhel, A.; Kosel, J. Magnetic Nanocomposite Cilia Tactile Sensor. *Adv. Mater.* **2015**, *27* (47), 7888–7892. https://doi.org/10.1002/adma.201504015.

(14) Martínez-Banderas, A. I.; Aires, A.; Teran, F. J.; Perez, J. E.; Cadenas, J. F.; Alsharif, N.; Ravasi, T.; Cortajarena, A. L.; Kosel, J. Functionalized Magnetic Nanowires for Chemical and Magneto-Mechanical Induction of Cancer Cell Death. *Sci. Rep.* **2016**, *6* (October), 1–11. https://doi.org/10.1038/srep35786.

(15) Mohammed, H.; Moreno, J. A.; Kosel, J. Advanced Fabrication and Characterization of Magnetic Nanowires. In *Magnetism and Magnetic Materials*; InTech, 2018; Vol. 2, pp 137–164. https://doi.org/10.5772/intechopen.71077.

(16) Mizeikis, V.; Mikulskas, I.; Tomašiunas, R.; Juodkazis, S.; Matsuo, S.; Misawa, H. Optical Characteristics of Two-Dimensional Photonic Crystals in Anodic Aluminum Oxide Films. *Japanese J. Appl. Physics, Part 1 Regul. Pap. Short Notes Rev. Pap.* **2004**, *43* (6 A), 3643–3647. https://doi.org/10.1143/JJAP.43.3643.

(17) Zhang, Z.; Zhang, L.; Hedhili, M. N.; Zhang, H.; Wang, P. Plasmonic Gold Nanocrystals Coupled with Photonic Crystal Seamlessly on TiO 2 Nanotube Photoelectrodes for Efficient Visible Light Photoelectrochemical Water Splitting. *Nano Lett.* **2013**, *13* (1), 14–20. https://doi.org/10.1021/nl3029202.

(18) Qiu, Y.; Leung, S.-F.; Zhang, Q.; Hua, B.; Lin, Q.; Wei, Z.; Tsui, K.; Zhang, Y.; Yang, S.; Fan, Z. Efficient Photoelectrochemical Water Splitting with Ultrathin Films of Hematite on Three-Dimensional Nanophotonic Structures. *Nano Lett.* **2014**, *14* (4), 2123–2129. https://doi.org/10.1021/nl500359e.

(19) Mao, A.; Han, G. Y.; Park, J. H. Synthesis and Photoelectrochemical Cell Properties of Vertically Grown α-Fe2O3 Nanorod Arrays on a Gold Nanorod Substrate. *J. Mater. Chem.* **2010**, *20* (11), 2247. https://doi.org/10.1039/b921965j.

(20) Mao, A.; Shin, K.; Kim, J. K.; Wang, D. H.; Han, G. Y.; Park, J. H. Controlled Synthesis of Vertically Aligned Hematite on Conducting Substrate for Photoelectrochemical Cells: Nanorods versus Nanotubes. *ACS Appl. Mater. Interfaces* **2011**, *3* (6), 1852–1858. https://doi.org/10.1021/am200407t.

(21) Murphy, A. B.; Barnes, P. R. F.; Randeniya, L. K.; Plumb, I. C.; Grey, I. E.; Horne, M. D.; Glasscock, J. A. Efficiency of Solar Water Splitting Using Semiconductor Electrodes. *Int. J. Hydrogen Energy* **2006**, *31* (14), 1999–2017. https://doi.org/10.1016/j.ijhydene.2006.01.014.

(22) Masuda, H. and M. S. Fabrication of Gold Nanodot Array Using Anodic Porous Alumina as an Evaporation Mask. **1996**, *126*.

(23) Sulka, G. D.; Brzózka, A.; Zaraska, L.; Wierzbicka, E.; Brudzisz, A. AAO Templates with Different Patterns and Channel Shapes. In *Submicron Porous Materials*; Springer International Publishing: Cham, 2017; pp 107–156. https://doi.org/10.1007/978-3-319-53035-2_5.

(24) Di Bari, G. A. Electrodeposition of Nickel. In *Modern Electroplating*; Milan, E., Ed.; John Wiley & Sons, Inc.: Hoboken, NJ, USA, 2011; pp 79–114. https://doi.org/10.1002/9780470602638.ch3.

(25) ASM International. Thermal Expansion. In *ASM Ready Reference: Thermal Properties of Metals*; ASM International, 2002.

(26) Li, J.; Malis, T.; Dionne, S. Recent Advances in FIB–TEM Specimen Preparation Techniques. *Mater. Charact.* **2006**, *57* (1), 64–70. https://doi.org/https://doi.org/10.1016/j.matchar.2005.12.007.

(27) Kay, A.; Cesar, I.; Grätzel, M. New Benchmark for Water Photooxidation by Nanostructured α-Fe 2O3 Films. *J. Am. Chem. Soc.* **2006**, *128* (49), 15714–15721. https://doi.org/10.1021/ja064380l.

(28) Schneider, C. A.; Rasband, W. S.; Eliceiri, K. W. NIH Image to ImageJ: 25 Years of Image Analysis. *Nat. Methods* **2012**, *9* (7), 671–675. https://doi.org/10.1038/nmeth.2089.

(29) PILLING; B., N. The Oxidation of Metals at High Temperature. *J. Inst. Met.* **1923**, *29*, 529–582.

(30) Le Formal, F.; Pendlebury, S. R.; Cornuz, M.; Tilley, S. D.; Gr??tzel, M.; Durrant, J. R. Back Electron-Hole Recombination in Hematite Photoanodes for Water Splitting. *J. Am. Chem. Soc.* **2014**, *136* (6), 2564–2574. https://doi.org/10.1021/ja412058x.

(31) Sivula, K.; Le Formal, F.; Grätzel, M. Solar Water Splitting: Progress Using Hematite (α-Fe 2O3) Photoelectrodes. *ChemSusChem* **2011**, *4* (4), 432–449. https://doi.org/10.1002/cssc.201000416.

(32) Wang, C. W.; Yang, S.; Fang, W. Q.; Liu, P.; Zhao, H.; Yang, H. G. Engineered Hematite Mesoporous Single Crystals Drive Drastic Enhancement in Solar Water Splitting. *Nano Lett.* **2016**, *16* (1), 427–433. https://doi.org/10.1021/acs.nanolett.5b04059.

(33) de Faria, D. L. A.; Venâncio Silva, S.; de Oliveira, M. T. Raman Microspectroscopy of Some Iron Oxides and Oxyhydroxides. *J. Raman Spectrosc.* **2005**, *28* (11), 873–878. https://doi.org/10.1002/(sici)1097-4555(199711)28:11<873::aid-jrs177>3.0.co;2-b.

(34) Sartoretti, C. J.; Alexander, B. D.; Solarska, R.; Rutkowska, I. A.; Augustynski, J.; Cerny, R. Photoelectrochemical Oxidation of Water at Transparent Ferric Oxide Film Electrodes. *J. Phys. Chem. B* **2005**, *109* (28), 13685–13692. https://doi.org/10.1021/jp051546g.

(35) Serrano, A.; Rubio-Zuazo, J.; López-Sánchez, J.; Arnay, I.; Salas-Colera, E.; Castro, G. R. Stabilization of Epitaxial α-Fe2O3 Thin Films Grown by Pulsed Laser Deposition on Oxide Substrates. *J. Phys. Chem. C* **2018**, *122* (28), 16042–16047.

https://doi.org/10.1021/acs.jpcc.8b02430.

(36) Jubb, A. M.; Allen, H. C. Vibrational Spectroscopic Characterization of Hematite, Maghemite, and Magnetite Thin Films Produced by Vapor Deposition. *ACS Appl. Mater. Interfaces* **2010**, *2* (10), 2804–2812. https://doi.org/10.1021/am1004943.

(37) Krajewski, M.; Gołasa, K.; Wasik, D. Influence of Iron Nanowires Oxidation on Their Semiconducting Properties. *Acta Phys. Pol. A* **2016**, *129* (1), A135–A137. https://doi.org/10.12693/APhysPolA.129.A-135.

(38) Colliex, C.; Manoubi, T.; Ortiz, C. Electron-Energy-Loss-Spectroscopy near-Edge Fine Structures in the Iron-Oxygen System. *Phys. Rev. B* **1991**, *44* (20), 11402–11411. https://doi.org/10.1103/PhysRevB.44.11402.

(39) Wang, C.; Baer, D. R.; Amonette, J. E.; Engelhard, M. H. Morphology and Electronic Structure of the Oxide Shell on the Surface of Iron Nanoparticles - Journal of the American Chemical Society (ACS Publications). **2009**, No. 5, 8824–8832. https://doi.org/10.1021/ja900353f.

(40) Laurence A. J. Garvie; Craven, A. J.; Brydson, R. Use of Electron-Energy Loss near-Edge Fine Structure in the Study of Minerals. *Am. Mineral.* **1994**, *79* (5–6), 411–425.

(41) Cavé, L.; Al, T.; Loomer, D.; Cogswell, S.; Weaver, L. A STEM/EELS Method for Mapping Iron Valence Ratios in Oxide Minerals. *Micron* **2006**, *37* (4), 301–309. https://doi.org/10.1016/j.micron.2005.10.006.

(42) Gunay, H. B.; Ghods, P.; Isgor, O. B.; Carpenter, G. J. C.; Wu, X. Characterization of Atomic Structure of Oxide Films on Carbon Steel in Simulated Concrete Pore Solutions Using EELS. *Appl. Surf. Sci.* **2013**, *274*, 195–202. https://doi.org/10.1016/j.apsusc.2013.03.014.

(43) Ivanov, Y. P.; Alfadhel, A.; Alnassar, M.; Perez, J. E.; Vazquez, M.; Chuvilin, A.; Kosel, J. Tunable Magnetic Nanowires for Biomedical and Harsh Environment Applications. *Sci. Rep.* **2016**, *6* (March), 24189. https://doi.org/10.1038/srep24189.

(44) Wang, Z.; Li, C.; Domen, K. Recent Developments in Heterogeneous Photocatalysts for Solar-Driven Overall Water Splitting. *Chem. Soc. Rev.* **2019**, *48*

(7), 2109–2125. https://doi.org/10.1039/c8cs00542g.

(45) Hisatomi, T.; Kubota, J.; Domen, K. Recent Advances in Semiconductors for Photocatalytic and Photoelectrochemical Water Splitting. *Chem. Soc. Rev.* **2014**, *43* (22), 7520–7535. https://doi.org/10.1039/c3cs60378d.

(46) Gurudayal; Bassi, P. S.; Sritharan, T.; Wong, L. H. Recent Progress in Iron Oxide Based Photoanodes for Solar Water Splitting. *J. Phys. D. Appl. Phys.* **2018**, *51* (47). https://doi.org/10.1088/1361-6463/aae138.

(47) Li, C.; Luo, Z.; Wang, T.; Gong, J. Surface, Bulk, and Interface: Rational Design of Hematite Architecture toward Efficient Photo-Electrochemical Water Splitting. *Adv. Mater.* **2018**, *1707502* (001), 1–23. https://doi.org/10.1002/adma.201707502.

(48) Cabrera, N.; Mott, N. F. Theory of the Oxidation of Metals. *Reports Prog. Phys.* **1949**, *12* (1), 308. https://doi.org/10.1088/0034-4885/12/1/308.

(49) Wang, C. M.; Baer, D. R.; Thomas, L. E.; Amonette, J. E.; Antony, J.; Qiang, Y.; Duscher, G. Void Formation during Early Stages of Passivation: Initial Oxidation of

Iron Nanoparticles at Room Temperature. *J. Appl. Phys.* **2005**, *98* (9). https://doi.org/10.1063/1.2130890.

(50) Nakamura, R.; Matsubayashi, G.; Tsuchiya, H.; Fujimoto, S.; Nakajima, H. Formation of Oxide Nanotubes via Oxidation of Fe, Cu and Ni Nanowires and Their Structural Stability: Difference in Formation and Shrinkage Behavior of Interior Pores. *Acta Mater.* **2009**, *57* (17), 5046–5052. https://doi.org/10.1016/j.actamat.2009.07.006.

(51) El Mel, A. A.; Nakamura, R.; Bittencourt, C. The Kirkendall Effect and Nanoscience: Hollow Nanospheres and Nanotubes. *Beilstein J. Nanotechnol.* **2015**, *6* (1), 1348–1361. https://doi.org/10.3762/bjnano.6.139.

(52) Kirkendall, E.; Thomassen, L.; Uethegrove, C. Rates of Diffusion of Copper and Zinc in Alpha Brass. *Trans. Am. Inst. Min. Metall. Eng.* **1939**, *133* (967), 186–203.

(53) Van Orman, J. A.; Crispin, K. L. Diffusion in Oxides. *Rev. Mineral. Geochemistry* **2010**, *72* (1), 757–825. https://doi.org/10.2138/rmg.2010.72.17.

(54) Eveno, P.; Paulus, M. Diffusion of Ni 63 in Ferrite Mixtures of Fe and Ni. *Phys. Status Solidi* **1974**, *22* (2), 569--577.

(55) Hirano, K.; Cohen, M.; Averbach, B. L. Diffusion of Nickel into Iron. *Acta Metall.* **1961**, *9* (5), 440–445. https://doi.org/10.1016/0001-6160(61)90138-9.

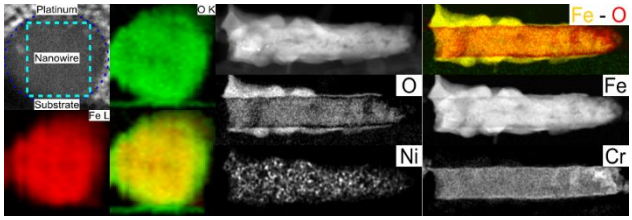

For Table of Contents Only